Fast Assessment Method for Minimum Demand Inertia in Power Systems

Qili Ding, Xinggan Zhang, Zifeng Li, Xiangxu Wang, and Weidong Li

***Abstract*—The existing minimum demand inertia (MDI) assessment methods based on time-domain simulation of system frequency response are complex in modeling and time-consuming in computation. If incorporating the load-side resources, it will lead to further computation inefficiency. This paper proposes a fast assessment method (FAM) for MDI in power systems. A full-response analytical model (FRAM) of a multi-resource system considering the load-side inertia is developed. The analytical expression of the mapping relationship between the maximum frequency deviation and system inertia is derived, thus realizing the fast solution of the system MDI under frequency security constraints. Case studies based on the modified IEEE RTS-79 test system and a provincial power grid in China demonstrate that the proposed FAM can solve the MDI in milliseconds without being affected by the system scale while maintaining high accuracy. This can provide an accurate and rapid analytical tool for sensing inertia security boundary in grid inertia resource planning and operation scheduling.**

***Index Terms*—Fast assessment method (FAM), inertia estimation, minimum demand inertia (MDI), security boundary, load-side resource, time-domain simulation, frequency response.**

NOMENCLATURE

$\alpha_G(t), \beta_G(t)$	Time representation coefficient and its integral of conventional unit
$\alpha_a(t), \beta_a(t)$	Time representation coefficient and its integral of grid-following inverter-based resource (GFL-IBR)
$\alpha_b(t), \beta_b(t)$	Time representation coefficient and its integral of grid-forming inverter-based resource (GFM-IBR)
$\Delta\omega$	Change in angular velocity of system
$\varepsilon(t), \delta(t)$	Step function and impulse function
b_g, c_g	Constants of gas turbine unit (GTU) valve positioner
$f, \Delta f$	System frequency and its deviation
Δf_{max}	The maximum frequency deviation
F_H	Power ratio coefficient of high-pressure turbine
H_{am}	Inertia time constant of induction motor (IM)
H_{GFM}	Virtual inertia coefficient of GFM-IBR
H_{min}	The minimum demand inertia
H_s, D_s	System inertia constant and damping coefficient of each type of resource
$H_{i,m}, R_{i,m}$	Inertia constant and modulation coefficient of unit m in the i^{th} type of resource
i, m	Indices of type of resources and units
I_1, I_2, I_3	Frequency response coefficients of IM
I_m	Parameter to be aggregated for inverter-based resource (IBR) m
$k_{new,m}$	Equivalent gain parameter of IBR m
K, T	Fitted parameters for conventional unit
K_a, T_a	Fitted parameters for GFL-IBR
K_b, T_b	Fitted parameters for IM
K_G, K_H, K_T	Capacity proportion coefficients for GTU, hydro power unit (HPU), and thermal power unit (TPU)
K_{GFM}, K_{GFL}	Capacity proportion coefficients for GFM-IBR and GFL-IBR
$K_{i,m}$	Capacity ratio of unit m in the i^{th} type of resource
K_M	Capacity proportion coefficient of IM
K_{VI}, R_{VI}	Virtual inertia coefficient and virtual sag coefficient for GFL-IBR
L	Number of resource types
N_G, N_H, N_T	Total numbers of GTUs, HPUs, and TPUs
N_i	Number of units in the i^{th} type of resource
N_{new}, N_M	Total numbers of IBRs and IMs
ΔP_L	Load-shedding power
ΔP_e	Electromagnetic power increment
ΔP_G	Active output increment of conventional unit
ΔP_g	Difference between mechanical power and load power
$\Delta P_M, \Delta P_N$	Active output increments of IM and GFL-IBR

Manuscript received: January 4, 2025; revised: March 20, 2025; accepted: June 11, 2025. Date of CrossCheck: June 11, 2025. Date of online publication: July 7, 2025.

This work was supported by National Natural Science Foundation of China (No. U22A20223).

Q. Ding, X. Zhang, and W. Li (corresponding author) are with School of Electrical Engineering, Dalian University of Technology, Dalian 116024, China (e-mail: qlding01@163.com; xingganz@163.com; wdli@dlut.edu.cn).

Z. Li is with Dalian Electric Power Supply Company of State Grid Liaoning Electric Power Supply Co., Ltd., Dalian 116001, China (e-mail: nedulzf@163.com).

X. Wang is with Electric Power Research Institute of State Grid Liaoning Electric Power Supply Co., Ltd., Shenyang 110000, China (e-mail: 535762230@qq.com).

DOI: 10.35833/MPCE.2025.000010

R_G, R_H, R_T	Modulation coefficients of GTU, HPU, and TPU
R_{GFM}, H_{GFM}	Virtual modulation coefficient and virtual inertia coefficient of GFM-IBR
s	Complex variable in Laplace transformation
t_n	Time to the maximum frequency deviation
t_0	Moment of load-side power support
T_C	Time constant of steam turbine
T_{CD}	Time constant of compressor discharge volume
T_{CR}	Time constant of combustion reaction delay
T_D, T_{GFM}	Response time of constants of GFL-IBR and GFM-IBR
T_F	Time constant of GTU fuel
T_G	Time constant of gas capacity
T_R	Time constant of reheater
T_{RH}	Transient droop time constant of HPU governor
T_{RS}	Reset time constant of HPU governor
T_W	Time constant of water hammer effect
T_y	Response time constant of contactor
X_g	Lead time constant of GTU governor
Y_g	Lag time constant of GTU governor

I. Introduction

THE power system inertia is crucial for maintaining system frequency stability. Excessively low inertia results in inadequate system anti-disturbance capability, seriously threatening the secure and stable operation of power grids [1]. Specifically, insufficient inertia may cause two critical issues. First, the system disturbances can trigger excessive rate of change of frequency (RoCoF), which risks tripping distributed generation units and damaging synchronous machines [2]. Second, the critically low inertia accelerates the occurrence and amplifies the magnitude of the maximum frequency deviation (MFD), potentially leading to grid frequency collapse before frequency regulation mechanisms are activated [3]. Insufficient system inertia may directly trigger rapid deterioration of both RoCoF and MFD following grid disturbances, ultimately culminating in frequency collapse accidents such as the UK's "8.9" blackout [4] and South Australia's "9.28" blackout [5].

With the accelerated construction of modern power systems, the proportion of renewable energy sources such as wind power, photovoltaic (PV) generation, and energy storage is increasing. At the same time, traditional synchronous units are gradually replaced, resulting in a continuously decreasing trend of system synchronous inertia [6]. ENTSO-E and WECC have predicted that the grid inertia will be further reduced in the future and the power system will exhibit significant low-inertia characteristics [7], [8]. Consequently, the frequency stability situation of the power system is becoming increasingly severe, with the risk of frequency instability continuing to escalate. Therefore, the accurate assessment of inertia level and inertia demand in power systems has become critical in grid operation and planning.

The minimum demand inertia (MDI) assessment constitutes an essential component of system operational analysis. It can provide the fundamental basis for sensing the inertia security boundary during the planning, allocation, and operational scheduling of grid inertia resources. This ensures that the system maintains adequate anti-disturbance capability to reduce the frequency instability risks following system disturbances, thus guaranteeing the system operational security.

The system MDI represents the minimum required inertia level that must be maintained during anticipated disturbances to ensure that all frequency dynamic indicators remain within the predefined frequency security constraints. Regarding the MDI assessment, some relevant studies have been carried out. References [9] and [10] propose an MDI assessment method considering RoCoF constraints, where the MDI is calculated from the disturbance power and RoCoF constraints. These RoCoF-based methods fail to account for MFD constraints, which may lead to a deviation of the assessment results from reality. Reference [11] considers the synchronous inertia constraint in economic dispatch, where the system MDI under the dual constraints of RoCoF and MFD is derived by iterative simulation. References [12] and [13] iteratively solve the system MDI under the frequency dynamic constraints based on the frequency response simulation model (FRSM). Reference [14] optimally solves the system MDI under the dual frequency constraints based on the improved grey wolf optimization (GWO) algorithm. Reference [15] further considers the impact of frequency spatial distribution on MDI assessment in the optimization model. Such methods based on the iterative simulation and optimization need to track the frequency security constraints by simulation or numerical integration to ensure high computational accuracy, and thus may reduce their computational efficiency. References [16] and [17] directly solve the power system MDI under the MFD constraints based on the reduced analytical frequency response model, which is efficient in computation, although the linearized approximation process may lead to reduction in its computational accuracy. Table I compares different studies on MDI assessment. Current research on MDI assessment primarily focuses on RoCoF and MFD as key constraints, employing the system FRSM or reduced analytical frequency response model to solve system MDI under dual constraints. These established methods provide substantial theoretical foundations for power system MDI assessment.

However, with the increasing computational efficiency requirements in system operation and management, coupled with the growing integration of load-side resources, the existing MDI assessment methods face problems in two aspects.

1) The diversity and scale of frequency regulation resources in modern power grids lead to high-order, strongly coupled, and nonlinear characteristics in system FRSM. Consequently, the FRSM-based MDI assessment methods suffer from complex model construction and computational inefficiency, failing to meet escalating computational efficiency requirements. Moreover, these complex system characteristics

hinder the accurate analytical expression of frequency responses, rendering existing analytical model-based MDI assessment methods unable to meet the computational accuracy requirements.

2) Most existing MDI assessment methods neglect the inertia capacity of load-side resources, resulting in deviations of the assessment results from actual values, thus posing potential security risks [18], [19]. The consideration of massive and distributed load-side resources with heterogeneous characteristics would significantly increase model complexity in FRSM-based MDI assessment, further degrading computational efficiency. Existing analytical model-based MDI assessment methods would also experience additional accuracy deterioration. For large-scale power systems with numerous operational scenarios, these limitations render existing MDI assessment methods inadequate for meeting the fast and accurate computational requirements for grid operation management and real-time control.

TABLE I
COMPARISON OF DIFFERENT STUDIES ON MDI ASSESSMENT

Reference	Solving method	Considered load-side resource	Efficiency and computational accuracy	Form of frequency security constraint
[9], [10]	Based on rotor motion equation	None	Efficient but neglecting MFD constraints	Analytical expression
[11], [13]	Based on iterative simulation	None	Inefficient but with relatively high accuracy	Tracking by simulation
[12]	Based on iterative simulation	Induction motor (IM)	Inefficient but with relatively high accuracy	Tracking by simulation
[14], [15]	Based on optimization	None	Inefficient but with relatively high accuracy	Numerical integration
[16]	Based on reduced analytical model	None	Efficient but with relatively low accuracy	Analytical expression
[17]	Based on reduced analytical model	Emergency interruptible load (EIL)	Efficient but with relatively low accuracy	Analytical expression
This paper	Based on FRSM	IM and EIL	Efficient while ensuring high accuracy	Analytical expression

To address these problems, this paper proposes a fast assessment method (FAM) for MDI considering the inertia support capacity from multiple types of regulation resources. The full-response analytical model (FRAM) of MFD is established based on the superposition theorem. Then, the fast solution of the system MDI is realized by the analytical expression of the mapping relationship between the MFD and system inertia. Compared with existing MDI assessment methods, the main contributions of this paper are as follows.

1) The proposed FAM can achieve millisecond-level computation speeds regardless of system scale. While maintaining the high solution accuracy, the proposed FAM significantly enhances the solving efficiency of MDI, thereby providing a faster and more accurate basis for sensing grid inertia security boundary in resource planning and allocation.

2) The proposed FAM effectively considers the impact of load-side resources, such as EIL and IM, on MDI assessment, yielding results that better match actual grid conditions than existing MDI assessment methods. Moreover, it avoids constructing complex simulation models by using straightforward solution steps that are easy to implement, making it more suitable for practical engineering applications.

3) An FRAM of the multi-resource system is developed, which accounts for secondary disturbances (caused by load-side power support). This model enables the fast calculation of MFD and the analytical expression of MFD constraints in MDI assessment.

The remainder of this paper is organized as follows. The FRAM of the multi-resource system is developed in Section II. The proposed FAM for MDI is presented in Section III. Case studies and simulation results are presented in Section IV. Conclusions are drawn in Section V.

II. CONSTRUCTION OF FRAM OF MULTI-SOURCE SYSTEM

A. Analysis of Frequency Dynamic Constraints

The MDI represents the minimum inertia required by the system to ensure that the RoCoF and MFD do not exceed their specified constraints, i.e., $Rof_{\lim}$ and $\Delta f_{\lim}$, respectively, under the anticipated disturbance ΔP_{d}. Therefore, if the mapping relationship among MDI, $Rof_{\lim}$, and $\Delta f_{\lim}$ can be found and an explicit analytical expression can be derived, the direct and fast assessment of MDI can be realized by solving the equations.

The frequency characteristics of the system can be expressed by the equivalent rotor motion equation [20] as:

$$2H_{\mathrm{s}}\frac{\mathrm{d}f}{\mathrm{d}t}+D_{\mathrm{s}}\Delta f=\Delta P_{\mathrm{d}} \tag{1}$$

If the system load damping is neglected, the RoCoF depends solely on the disturbance power and system inertia. In low-inertia systems, the system RoCoF reaches its maximum at the instant of disturbance. Therefore, under the RoCoF constraint, the system MDI can be solved analytically [13] as:

$$H_{\min}=\Delta P_{\mathrm{d}}/(2\cdot Rof_{\lim}) \tag{2}$$

Regarding the MFD constraint, the system MFD depends on the disturbance magnitude and system inertia, and is also closely related to the primary frequency regulation capability of system. To realize the fast assessment of system MDI under the MFD constraint, it is necessary to establish an analytical frequency response model to obtain the explicit analytical expression between the MFD and system inertia. This explicit relationship can be expressed using function $f(\cdot)$ as:

$$\Delta f_{\max}=f(\Delta P_{\mathrm{d}},H_{\mathrm{s}}) \tag{3}$$

Based on this explicit analytical expression, the system MDI under the MFD constraint can be solved using the inverse function of $f(\cdot)$, i.e., $g(\cdot)$.

$$H_{\min}=g(\Delta P_{\mathrm{d}},\Delta f_{\lim}) \tag{4}$$

Based on the analysis of frequency dynamic constraints, it is evident that the key to the fast assessment of system MDI lies in establishing an analytical frequency response model to achieve the analytical expression of MFD.

It should be noted that the MDI solved in this paper is oriented to the system as a whole. Therefore, the spatial distribution of frequency is neglected, and the frequency of the center of inertia (CoI) is utilized for modeling and calculation [21], [22].

B. Construction of Aggregated Model

To address the high-order and nonlinear characteristics of the FRSM, the response models of each type of resource need to be aggregated to reduce the order of FRSM. At the same time, considering that each type of resource should maintain sufficient reserve capacity to participate in the frequency response [23], the power constraint module is ignored in this paper.

1) Aggregation of Conventional Units

Conventional units primarily include thermal power units (TPUs), hydro power units (HPUs), and gas turbine units (GTUs), whose frequency response characteristics are shown in Fig. 1 [24], [25].

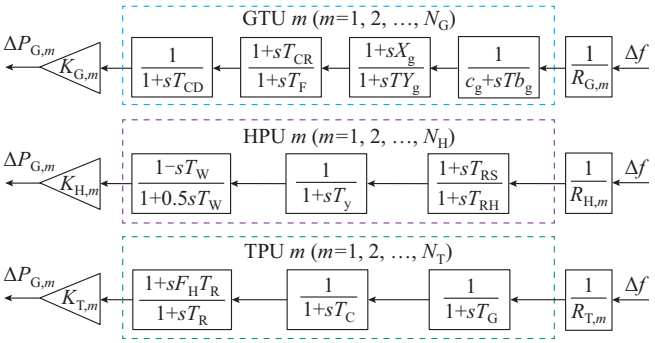

Fig. 1. Frequency response model of conventional units.

To reduce the order of FRSM, multiple units of the same type are aggregated into one equivalent unit. Taking HPU as an example, the governor parameter $Y\in\{T_{\mathrm{W}},T_{\mathrm{y}},T_{\mathrm{RS}},T_{\mathrm{RH}}\}$ can be aggregated based on the principle of branch standardized gain aggregation [26]:

$$Y=\sum_{m=1}^{N_{\mathrm{H}}}Y_mK_{\mathrm{H},m}\Big/\left(R_{\mathrm{H},m}\sum_{m=1}^{N_{\mathrm{H}}}K_{\mathrm{H},m}/R_{\mathrm{H},m}\right) \tag{5}$$

Similarly, multiple TPUs and GTUs can be aggregated into equivalent single units. Based on the principle of branch standardized gain aggregation, let $X\in\{T_{\mathrm{G}},T_{\mathrm{C}},F_{\mathrm{H}},T_{\mathrm{R}}\}$ and $Z\in\{c_{\mathrm{g}},b_{\mathrm{g}},X_{\mathrm{g}},Y_{\mathrm{g}},T_{\mathrm{CR}},T_{\mathrm{F}},T_{\mathrm{CD}}\}$, and then we have:

$$X=\sum_{m=1}^{N_{\mathrm{T}}}X_mK_{\mathrm{T},m}\Big/\left(R_{\mathrm{T},m}\sum_{m=1}^{N_{\mathrm{T}}}K_{\mathrm{T},m}/R_{\mathrm{T},m}\right) \tag{6}$$

$$Z=\sum_{m=1}^{N_{\mathrm{G}}}Z_mK_{\mathrm{G},m}\Big/\left(R_{\mathrm{G},m}\sum_{m=1}^{N_{\mathrm{G}}}K_{\mathrm{G},m}/R_{\mathrm{G},m}\right) \tag{7}$$

2) Aggregation of Renewable Energy Units

In modern power systems, renewable energy units such as wind turbine (WT) unit, PV unit, and energy storage unit can provide inertia and primary frequency regulation capability to the grid through inverter-based devices with control logic [27]. Although these inverter-based resources (IBRs) operate in different generation modes, the essence of their participation in the frequency response process remains the same. Depending on the grid-connection modes and control strategies, IBRs can be categorized into grid-following IBR (GFL-IBR) and grid-forming IBR (GFM-IBR) [28].

GFM-IBR can not only simulate the external characteristics of the synchronous machine through the virtual synchronous generator (VSG) control [29], but also actively establish frequency and have grid-forming ability, making it equivalent to a synchronous unit. GFL-IBR participates in frequency regulation through virtual inertia control and virtual droop control, with a certain time delay in its control response. The frequency response model of IBRs is illustrated in Fig. 2 [30], [31], where GFL-IBR lacks grid-forming capability, so its inertia cannot be directly equivalent to the overall system inertia; and GFM-IBR can be equivalent to a synchronous unit, and its inertia is directly incorporated into the system inertia.

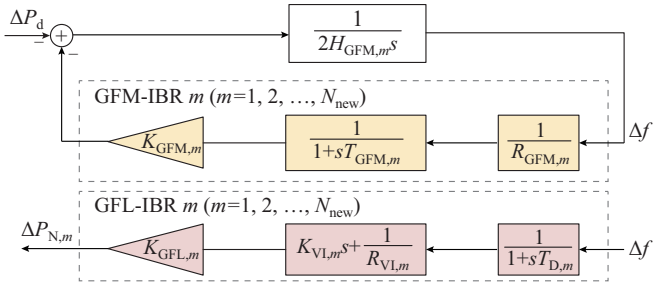

Fig. 2. Frequency response model of IBRs.

For renewable energy units, whether GFM-IBR or GFL-IBR, the branch standardized gain aggregation can be used to aggregate multiple units into equivalent single units. Let $I\in\{T_{\mathrm{GFM}},K_{\mathrm{VI}},R_{\mathrm{VI}},T_{\mathrm{D}}\}$, then:

$$I=\sum_{m=1}^{N_{\mathrm{new}}}I_mk_{\mathrm{new},m}\Big/\sum_{m=1}^{N_{\mathrm{new}}}k_{\mathrm{new},m} \tag{8}$$

where $k_{\mathrm{new},m}=K_{\mathrm{GFM},m}/R_{\mathrm{GFM},m}$ or $k_{\mathrm{new},m}=K_{\mathrm{GFL},m}/R_{\mathrm{VI},m}$.

3) Aggregation of Load-side Resources

Representative load-side resources with inertia and primary frequency regulation capability mainly include IM and flexible controllable loads. The rotor of IM is electromechanically coupled to the grid and can spontaneously respond to system disturbances by releasing the kinetic energy of the rotor, thus providing inertia support. The frequency response model of IM is shown in Fig. 3, and the related parameters can be referred to [18].

The frequency response transfer function of IM can be expressed as:

$$G_{\mathrm{M}}(s)=\frac{\Delta P_{\mathrm{e}}}{\Delta\omega}=\frac{I_1s+I_2}{2H_{\mathrm{am}}s+I_3} \tag{9}$$

Let $M\in\{H_{\mathrm{am}},I_1,I_2,I_3\}$, then:

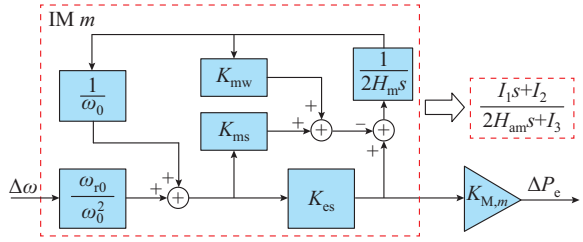

Fig. 3. Frequency response model of IM.

$$M=\sum_{m=1}^{N_M}\left(M_m K_{M,m}\Big/\sum_{m=1}^{N_M}K_{M,m}\right) \tag{10}$$

For flexible controllable loads, the mature load response strategy currently applied is mainly the active load-shedding control for EIL. This strategy actively cuts a certain amount of load to compensate for the system power deficit when the frequency drops, thereby maintaining system frequency stability [32], [33]. The response characteristics of active load-shedding mainly depend on the auxiliary service agreement between the grid and EIL provider and the load-shedding control strategy. The EIL considered in this paper employs the event-triggered control with a response delay to implement active load-shedding. The control logic is: after receiving a control command, the EIL sheds a load of ΔP_L after a response delay of t_0.

4) Construction of Multi-resource Aggregated Frequency Response Model (AFRM)

After aggregating the parameters of each type of regulation resource, the multi-resource AFRM can be established, as shown in Fig. 4.

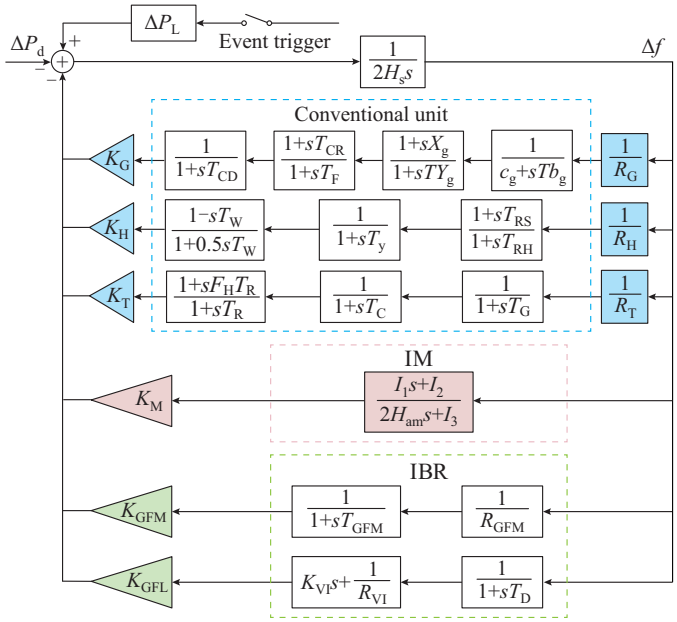

Fig. 4. Multi-resource AFRM.

The system inertia constant H_s and the modulation coefficients R_i of each type of resource after aggregation are calculated as:

$$H_s=\sum_{i=1}^{L}\sum_{m=1}^{N_i}K_{i,m}H_{i,m} \tag{11}$$

$$\frac{1}{R_i}=\sum_{m=1}^{N_i}\frac{K_{i,m}}{R_{i,m}} \tag{12}$$

For GFL-IBR, its inertia constant H_{GFL} is 0. For IM, its inertia constant H_{IM} is 0, and its modulation coefficient R_{IM} is 1.

C. Response Characteristic Fitting and Model Decoupling

1) Response Characteristic Fitting

In the AFRM, the transfer function of response characteristics for conventional units remains of high order. Their response characteristics can be fitted into a first-order inertia element and the fitting parameters can be obtained through the least-squares method [34]. The power-frequency characteristic in the complex frequency domain is expressed as:

$$\Delta P_{Gi}=\frac{-K_i}{1+T_i s}\Delta f \tag{13}$$

The response characteristic of GFM-IBR is a first-order inertia element, which can be regarded as a class of synchronous units. Equation (13) can also be applied to characterize the GFM-IBR, where its power-frequency static characteristic coefficient is given by $K_i=K_{GFM}/R_{GFM}$.

For GFL-IBR, its power-frequency characteristic can be derived from Fig. 2 as:

$$\Delta P_N=\frac{-K_a}{1+T_a s}\Delta f-K_N F_N\Delta f \tag{14}$$

where $K_N=K_{GFL}$; $F_N=K_{VI}/T_D$; $K_a=K_N(1/R_{VI}-F_N)$; and $T_a=T_D$.

For IM, its power-frequency characteristic can be obtained by further derivation of (9):

$$\Delta P_M=\frac{-K_b}{1+T_b s}\Delta f-K_M F_M\Delta f \tag{15}$$

where $F_M=0.5I_1/H_{am}$; $K_b=K_M(I_2/I_3-F_M)$; and $T_b=2H_{am}/I_3$.

2) Model Decoupling

The difficulty in the analytical expression for frequency deviation lies in the coupling between frequency and power in the FRSM. In this paper, the decoupling of frequency and power is achieved by inputting a simulated frequency deviation curve, resulting in the low-order open-loop AFRM, as shown in Fig. 5.

The closer the simulated frequency deviation curve is to the actual one, the smaller the calculation error. When the system is disturbed and triggers power support from load-side resources such as EIL, the system frequency response will experience a secondary power shock, resulting in a sudden change as illustrated in Fig. 6. This paper adopts the composite function proposed in [35] to simulate the frequency deviation curve, which can more accurately simulate the actual frequency deviation curve compared with the initial frequency tangent proposed in [34]. Additionally, the expression of the composite function is relatively simple, facilitating the subsequent analytical derivation and fast solution.

The time-domain expression of the simulated frequency deviation curve is [35]:

$$\Delta f(t)=-ate^{-bt} \tag{16}$$

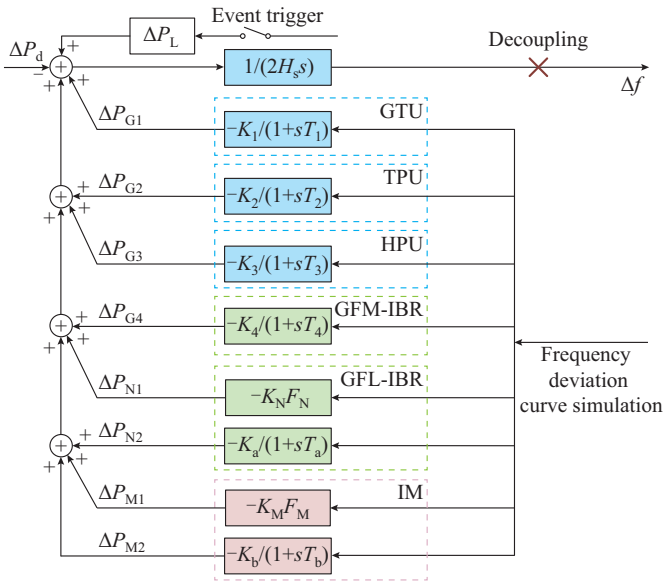

Fig. 5. Low-order open-loop AFRM.

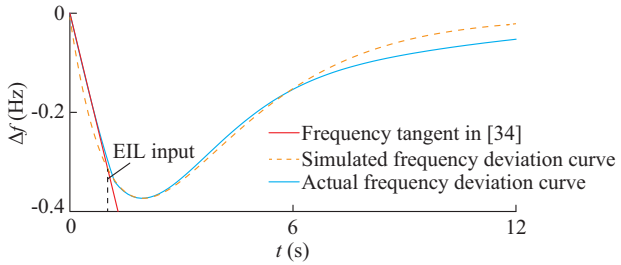

Fig. 6. Diagram of simulated frequency deviation curve.

Since the frequency deviation curve must pass through the frequency nadir $(t_n, \Delta f_{\max})$ and RoCoF is zero at the moment of t_n, the parameters can be derived as $a=\Delta P_{\mathrm{d}}/(2H_{\mathrm{s}})$ and $b=1/t_n$. Thus, the frequency-domain expression of the simulated frequency deviation curve can be obtained as:

$$\Delta f(s)=-\Delta P_{\mathrm{d}}/[2H_{\mathrm{s}}(s+1/t_n)^2] \tag{17}$$

By combining (17) with (13) and performing the Laplace transform, the time-domain expression for the active power of conventional unit i (including the GFM-IBR, which is treated as a synchronous unit) can be derived as:

$$\Delta P_{\mathrm{G}i}(t)=\frac{K_i\Delta P_{\mathrm{d}}t_n^2}{2H_{\mathrm{s}}}\left[\frac{T_i(\mathrm{e}^{-t/T_i}-\mathrm{e}^{-t/t_n})}{(T_i-t_n)^2}-\frac{t\mathrm{e}^{-t/t_n}}{t_n(T_i-t_n)}\right] \tag{18}$$

To facilitate the subsequent derivation, let:

$$\alpha_{\mathrm{G}i}(t)=\frac{T_i(\mathrm{e}^{-t/T_i}-\mathrm{e}^{-t/t_n})}{(T_i-t_n)^2}-\frac{t\mathrm{e}^{-t/t_n}}{t_n(T_i-t_n)} \tag{19}$$

For GFL-IBR and IM, their time-domain expressions of the active power can also be derived by combining (14), (15), and (17) as:

$$\Delta P_{\mathrm{N}}(t)=-\frac{K_{\mathrm{N}}F_{\mathrm{N}}\Delta P_{\mathrm{d}}t}{2H_{\mathrm{s}}}\mathrm{e}^{-\frac{t}{t_n}}+\frac{K_{\mathrm{a}}\Delta P_{\mathrm{d}}t_n^2}{2H_{\mathrm{s}}}\alpha_{\mathrm{a}}(t) \tag{20a}$$

$$\Delta P_{\mathrm{M}}(t)=-\frac{K_{\mathrm{M}}F_{\mathrm{M}}\Delta P_{\mathrm{d}}t}{2H_{\mathrm{s}}}\mathrm{e}^{-\frac{t}{t_n}}+\frac{K_{\mathrm{b}}\Delta P_{\mathrm{d}}t_n^2}{2H_{\mathrm{s}}}\alpha_{\mathrm{b}}(t) \tag{20b}$$

Based on (18) and (20), the active power of each type of resource can be obtained. Combined with Fig. 5, the time-domain expression of the system frequency following a disturbance can be derived as:

$$\sum_{i=1}^{4}\Delta P_{\mathrm{G}i}(t)+\Delta P_{\mathrm{N}}(t)+\Delta P_{\mathrm{M}}(t)+\Delta P_{\mathrm{L}}-\Delta P_{\mathrm{d}}=2H_{\mathrm{s}}\frac{\mathrm{d}f(t)}{\mathrm{d}t} \tag{21}$$

D. FRAM

The load-side power support induces a secondary power shock to the system frequency, leading to an abrupt change in the frequency curve. By assuming that the system is initially operating in the rated state, traditional frequency response analytical models analyze only the zero-state response process. Consequently, they fail to accurately solve the frequency deviation when considering load-side power support. In this paper, from the perspective of circuit theory, the zero-input response at the moment of load-side power support is integrated into the frequency response model. By applying the superposition theorem, the FRAM for MFD is established.

1) Zero-input Response

The zero-input response refers to the system response induced only by the preceding initial state without external excitation input. In the AFRM, ΔP_{G} and Δf reflect the states of the governor and rotor following a system disturbance, respectively. The zero-input response is mainly divided into two components: the governor side and rotor side. On the governor side, the time-domain expression for the active power of the conventional unit can be obtained by performing the inverse Laplace transform on (13):

$$-K_i\Delta f(t)=\Delta P_{\mathrm{G}i}(t)+T_i\frac{\mathrm{d}\Delta P_{\mathrm{G}i}(t)}{\mathrm{d}t} \tag{22}$$

If the initial state of the prime mover for conventional unit, i.e., $P_{\mathrm{G}i}(0^-)$, is considered, then by transforming (22) into the frequency domain, the frequency-domain expression for the active power of the conventional unit considering the initial state can be obtained as:

$$\Delta P_{\mathrm{G}i}=\frac{-K_i\Delta f+T_iP_{\mathrm{G}i}(0^-)}{1+T_is} \tag{23}$$

Similarly, the frequency-domain expressions for the active power of GFL-IBR and IM considering the initial states $P_{\mathrm{N}}(0^-)$ and $P_{\mathrm{M}}(0^-)$ can be derived as:

$$\Delta P_{\mathrm{N}}=\frac{-K_{\mathrm{a}}\Delta f+T_{\mathrm{a}}P_{\mathrm{N}}(0^-)}{1+T_{\mathrm{a}}s}-K_{\mathrm{N}}F_{\mathrm{N}}\Delta f+P_{\mathrm{N}}(0^-) \tag{24a}$$

$$\Delta P_{\mathrm{M}}=\frac{-K_{\mathrm{b}}\Delta f+T_{\mathrm{b}}P_{\mathrm{M}}(0^-)}{1+T_{\mathrm{b}}s}-K_{\mathrm{M}}F_{\mathrm{M}}\Delta f+P_{\mathrm{M}}(0^-) \tag{24b}$$

On the rotor side, if the initial state of the system rotor kinetic energy, i.e., $\Delta f(0^-)$, is considered, then by performing the inverse Laplace transform to (21), the frequency-domain expression of the system frequency can be derived as:

$$\Delta f=\frac{\Delta P_{\mathrm{g}}+2H_{\mathrm{s}}\Delta f(0^-)}{2H_{\mathrm{s}}s} \tag{25}$$

From the physical perspective, the initial states $P_{\mathrm{G}i}(0^-)$, $P_{\mathrm{N}}(0^-)$, and $P_{\mathrm{M}}(0^-)$ indicate that the unit increases its active

power based on the frequency deviation and the initial power state. Meanwhile, $\Delta f(0^-)$ indicates that the rotor regulates the real-time frequency according to the unit power and the initial frequency deviation.

2) Zero-state Response

The zero-state response refers to the response induced only by the external excitation ΔP_o without considering the initial state. According to (21), the time-domain expression of the system frequency under zero-state response can be derived as:

$$\sum_{i=1}^{4}\Delta P_{Gi}(t)+\Delta P_N(t)+\Delta P_M(t)-\Delta P_o=2H_s\frac{df(t)}{dt} \tag{26}$$

According to the superposition theorem, the system frequency full-response model (FFRM) can be obtained by superposing the zero-input response and zero-state response. By substituting (23), (24), and (25) into (26) after performing the inverse Laplace transform, the time-domain expression of the system frequency can be derived as:

$$\begin{aligned}2H_s\frac{df(t)}{dt}=&\sum_{i=1}^{4}\Delta P_{Gi}(t)+\Delta P_N(t)+\Delta P_M(t)-\Delta P_o+\\&\sum_{i=1}^{4}e^{-\frac{t}{T_i}}\Delta P_{Gi}(0^-)+e^{-\frac{t}{T_a}}P_N(0^-)+e^{-\frac{t}{T_b}}P_M(0^-)+\\&P_N(0^-)+P_M(0^-)+2H_s\Delta f(0^-)\delta(t)\end{aligned} \tag{27}$$

3) Analytical Solution of MFD

To achieve the explicit analytical expression for the frequency deviation, the FFRM needs to be further analyzed. Assume that the EIL provides power support to the system at moment t_0. Before t_0, the external excitation ΔP_{o1} is the system disturbance ΔP_d, and the system initial state is zero; After t_0, the external excitation ΔP_{o2} is the difference between ΔP_d and ΔP_L, and the system initial state consists of $P_{Gi}(0^-)$, $P_N(0^-)$, $P_M(0^-)$, and $\Delta f(0^-)$. Then, the time-domain full-response expression of frequency deviation, as shown in (28), can be obtained.

$$\begin{aligned}\Delta f(t)=&\left[\left(\sum_{i=1}^{4}K_i\beta_{Gi}(t)+K_a\beta_a(t)+K_b\beta_b(t)\right)\frac{\Delta P_{o1}t_n^2}{4H_s^2}+(K_NF_N+K_MF_M)\frac{\Delta P_{o1}}{4H_s^2}\int te^{-\frac{t}{t_n}}dt-\frac{\Delta P_{o1}}{2H_s}t\right](\varepsilon(t)-\varepsilon(t-t_0))+\\&\left[\left(\sum_{i=1}^{4}K_i\beta_{Gi}(t-t_0)+K_a\beta_a(t-t_0)+K_b\beta_b(t-t_0)\right)\frac{\Delta P_{o2}t_n^2}{4H_s^2}+(K_NF_N+K_MF_M)\frac{\Delta P_{o2}}{4H_s^2}\int(t-t_0)e^{-\frac{t-t_0}{t_n}}dt\right]\varepsilon(t-t_0)+\\&\left[\sum_{i=1}^{4}\int e^{-\frac{t-t_0}{T_i}}\frac{P_{Gi}(t_0^-)}{2H_s}dt+\int e^{-\frac{t-t_0}{T_a}}\frac{P_N(t_0^-)}{2H_s}dt+\int e^{-\frac{t-t_0}{T_b}}\frac{P_M(t_0^-)}{2H_s}dt+\frac{t-t_0}{2H_s}(P_N(t_0^-)+P_M(t_0^-)-\Delta P_{o2})+\Delta f(t_0^-)\right]\varepsilon(t-t_0)\end{aligned} \tag{28}$$

The expression for the frequency deviation curve after an abrupt change can be extracted from (28), and its derivative can be obtained as:

$$\begin{aligned}\frac{d\Delta f_2(t)}{dt}=&\frac{\Delta P_{o2}t_n^2}{4H_s^2}\left(\sum_{i=1}^{4}K_i\alpha_{Gi}(t)+K_a\alpha_a(t)+K_b\alpha_b(t)\right)+\\&\frac{\Delta P_{o2}te^{-\frac{t}{t_n}}}{4H_s^2}(K_NF_N+K_MF_M)-\frac{\Delta P_{o2}}{2H_s}+\sum_{i=1}^{4}\frac{e^{-\frac{t}{T_i}}}{2H_s}P_{Gi}(0^-)+\\&\frac{e^{-\frac{t}{T_a}}+1}{2H_s}P_N(0^-)+\frac{e^{-\frac{t}{T_b}}+1}{2H_s}P_M(0^-)+\Delta f(0^-)\delta(t)\end{aligned} \tag{29}$$

When the frequency response curve reaches its nadir, the RoCoF becomes zero; thus, (29) equals zero. Since (29) is timed from t_0, when (29) equals zero, $t=t_n-t_0$. At this time, the only unknown quantity t_n in (29) can be solved by making (29) equal to 0.

The MFD can be obtained by substituting t_n into (16):

$$\Delta f_{max}=-\frac{\Delta P_d}{2H_s}t_ne^{-1} \tag{30}$$

The analytical expression for the MFD with respect to inertia can be derived by establishing the FRAM. Under the anticipated disturbance, the MFD can be solved analytically based on the system inertia by (29) and (30).

Similarly, the corresponding MDI can be analytically determined in reverse for a given MFD constraint.

III. Proposed FAM for MDI

A. Solution for MDI

The direct and fast calculation of MDI under MFD constraint can be realized based on the explicit analytical expression for the frequency deviation. In this case, the quantities to be solved are t_n and H_{min}. A set of low-order quadratic equations can be established to solve them:

$$\begin{cases}\Delta f_{lim}=-\dfrac{\Delta P_d}{2H_{min}}t_ne^{-1}\\ \left.\dfrac{d\Delta f_2(t)}{dt}\right|_{t=t_n,H=H_{min}}=0\end{cases} \tag{31}$$

Under the MFD constraint, the specific steps of the proposed FAM are as follows.

Step 1: use (6) - (8) and (10) - (12) to aggregate various types of resources in the system into a single machine to establish the AFRM. Obtain the fitting parameters of the conventional units using the least-squares method.

Step 2: calculate the output of each unit at moment t_0 based on (17) and (20) to obtain the initial states $P_{Gi}(t_0^-)$, $P_N(t_0^-)$, and $P_M(t_0^-)$. Calculate the system frequency deviation at moment t_0 using (28) to obtain $\Delta f(t_0^-)$.

Step 3: substitute $P_{Gi}(t_0^-)$, $P_N(t_0^-)$, $P_M(t_0^-)$, and $\Delta f(t_0^-)$ into (29) and (31). Input the given Δf_{lim}, ΔP_d, and ΔP_L, and then solve H_{min} by using the vpaslove function in MATLAB.

Compared with the traditional MDI assessment method, the proposed FAM can quickly obtain the system MDI by solving a simple and low-order binary quadratic equation without establishing a complex simulation model. The calculation steps are straightforward to apply in practical engineering. Figure 7 illustrates the whole framework of the proposed FAM.

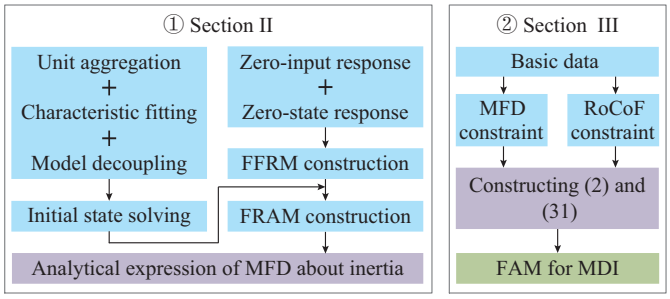

Fig. 7. Whole framework of proposed FAM.

B. Methods Used for Comparison Analysis

To validate the computational efficiency and accuracy of the proposed FAM, it is compared with the cyclic call approximation method (CCAM) and optimization solution method (OSM), which are based on the FRSM.

1) CCAM: set the initial inertia H_0 and iteration step dh. Iterate the system inertia starting from H_0 and call AFRM $F_{\text{AFRM}}(\cdot)$ to calculate $\Delta f_{\max}$. When the difference between $\Delta f_{\max}$ and $\Delta f_{\lim}$ is less than the stopping criterion ε, the corresponding inertia is the system MDI under the $\Delta f_{\lim}$ constraints.

2) OSM: take $H_{\min}$ as the decision variable, $\Delta f_{\lim}$ as the constraints, and the minimum absolute difference between $\Delta f_{\max}$ and $\Delta f_{\lim}$ as the optimization objective, an optimization model is established to solve the MDI. Intelligent optimization algorithms, such as the genetic algorithm or particle swarm algorithm, can be used to solve the optimization model, which can be expressed as:

$$\begin{cases} \min f(H_m) = \left| F_{\text{AFRM}}(\Delta P_{\text{d}}, H_m) - \Delta f_{\lim} \right| \\ \text{s.t. } F_{\text{AFRM}}(\Delta P_{\text{d}}, H_m) \le \Delta f_{\lim} \\ \quad 0 < H_m \le H_{\max} \end{cases} \tag{32}$$

Since AFRM needs to be called to solve the MFD, (32) is a nonlinear optimization model. In this paper, the MATLAB optimization toolbox fmincon is used for the solution.

IV. Case Studies

To validate the feasibility and validity of the proposed FAM for MDI and to analyze the impact of load-side power support on MDI, the modified IEEE RTS-79 test system and a provincial power grid in China are used for case studies. The model construction and solution are realized by MATLAB 2023b. The computer configuration includes an AMD Ryzen 5 5600GT CPU with Radeon Graphics and 32 GB of RAM.

A. Introduction to Case System

In the modified IEEE RTS-79 test system, the installed capacity and proportion of each unit can be referred to [36]. The installed system capacity is 3825 MW and the load is 2850 MW (where IM is 60 MW). Among them, the energy storage unit is GFM-IBR, with $H_{\text{GFM}} = 5$ s, $R_{\text{GFM}} = 10$, and $T_{\text{GFM}} = 0.05$ s. The WT and PV participate in frequency response by virtual droop control, with $R_{\text{VI}} = 10$ s and $T_{\text{D}} = 0.1$ s. The parameter values of the conventional units can be referred to [25].

In the provincial power grid, the relevant parameters of each unit are shown in Table II. The installed system capacity is 72541.2 MW and the load is 37500 MW (where IM is 700 MW). The governor type of nuclear power unit (NPU) is the same as that of TPU in the system, so it is modeled as a TPU.

TABLE II
Relevant Parameters of Each Unit

Unit	Capacity (MW)	Proportion (%)	Inertia time constant (s)
WT	14286.2	19.69	
PV	9576.6	13.20	
NPU	6675.2	9.20	13.30
HPU	3343.8	4.61	6.16
TPU	38559.4	53.16	6.35
Storage	100.0	0.14	5.00
Total	72541.2	100.00	4.89

B. Modified IEEE RTS-79 Test System

1) Computational Accuracy Analysis of FRAM

The accurate analytical expression of MFD is essential to ensure the accuracy of MDI assessment. To validate the computational accuracy of FRAM, its analysis results are compared with those of AFRM, the non-full response analytical model (non-FRAM), and the linear frequency deviation analytical model (LFAM). The non-FRAM refers to the analytical model that cannot consider the effects of secondary power disturbances.

Two disturbance scenarios are established. In Scenario 1, the disturbance is randomly sampled 100 times from 100 MW to 300 MW, while the load side provides 50 MW of power support with a time delay of 1 s. The MFD calculation results in Scenario 1 are compared in Fig. 8(a). In Scenario 2, the disturbance is set to be 300 MW, and the load-side power support is randomly sampled from 0 MW to 100 MW. The MFD calculation results in Scenario 2 are compared in Fig. 8(b).

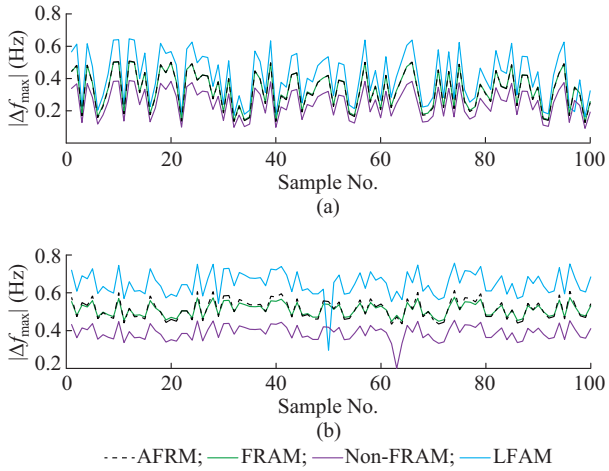

Fig. 8. Comparison of MFD calculation results. (a) Scenario 1. (b) Scenario 2.

As shown in Fig. 8, the results of FRAM are highly consistent with those of AFRM, while the non-FRAM and LFAM demonstrate significant computational deviations. To further validate the computational accuracy of FRAM, Fig. 9 gives the relative error (RE) of the three analytical models by taking the results of AFRM as the benchmark value. Figure 10 further compares the estimation performance of the three analytical models by mean absolute error (MAE), mean absolute percentage error (MAPE), and root mean square error (RMSE).

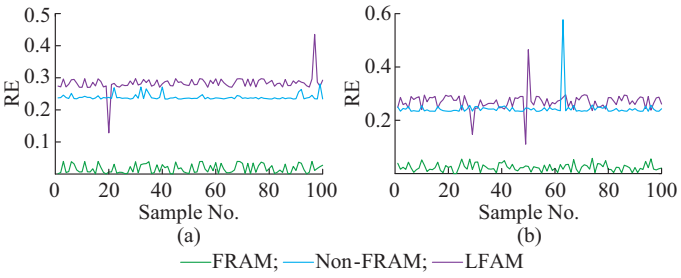

Fig. 9. RE of three analytical models. (a) Scenario 1. (b) Scenario 2.

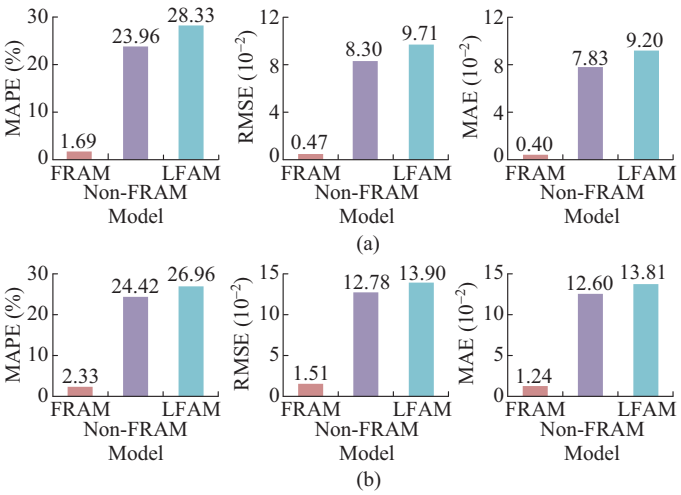

Fig. 10. MAPE, RMSE, and MAE of three analytical models. (a) Scenario 1. (b) Scenario 2.

The computational accuracy of FRAM is far higher than that of non-FRAM and LFAM, with its MAPE being 1.69% and 2.33% in Scenarios 1 and 2, respectively. This demonstrates its capability to accurately compute Δf_{max}. Moreover, the performance metrics of FRAM surpass those of non-FRAM and LFAM in both scenarios, highlighting its superior computational performance. Non-FRAM fails to consider the secondary power disturbances from the load side, resulting in underestimated calculation results with an MAPE exceeding 20%. The frequency deviation curve simulated by LFAM deviates significantly from the actual curve under load-side power support, resulting in substantial computational errors. The FRAM can realize the accurate calculation of MFD while considering the load-side power support, thereby effectively guaranteeing the accuracy of MDI assessment.

2) Analysis of Calculation Accuracy

To evaluate the computational performance of the proposed FAM for MDI, it is compared with CCAM and OSM. Two scenarios are established. Scenario 3: the disturbance is randomly sampled 100 times from 200 MW to 300 MW, and $\Delta f_{max} = 0.5$ Hz. The load side provides 50 MW of power support with a time delay of 1 s. The calculated MDIs in Scenario 3 are compared in Fig. 11(a). Scenario 4: the disturbance size is 300 MW, while the load-side power support is randomly sampled from 50 MW to 100 MW. The calculated MDIs in Scenario 4 are compared in Fig. 11(b). The iteration step of CCAM is 0.0001 s, and the stopping criterion is 0.0001 Hz.

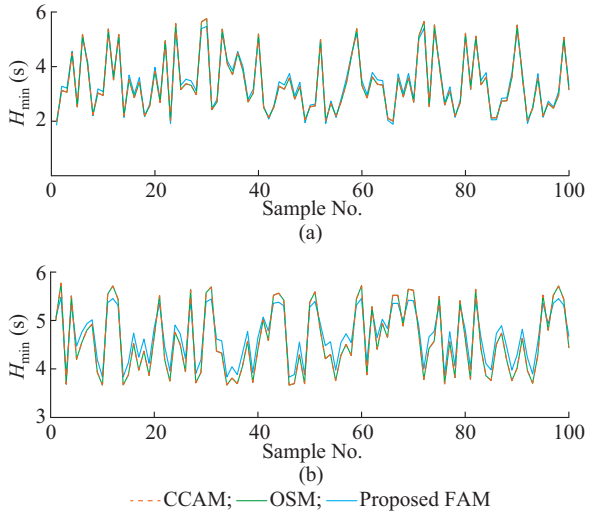

Fig. 11. Comparison of calculated MDIs. (a) Scenario 3. (b) Scenario 4.

From Fig. 11, the computational results of the proposed FAM are basically consistent with those of CCAM and OSM. And the computational results of CCAM and OSM exhibit high agreement, with average absolute errors of 0.27 ms and 0.248 ms in Scenarios 3 and 4, respectively. Since CCAM continuously approximates the system MDI by cyclically calling the simulation model, its results are theoretically closest to the real value. Due to the limited precision of its iteration step and stopping criterion, there remains a minor error relative to OSM. The optimization model of OSM is convex, ensuring that its computational result represents the global optimum. Figure 12 gives the REs of proposed FAM by taking the computational results of OSM as the benchmark.

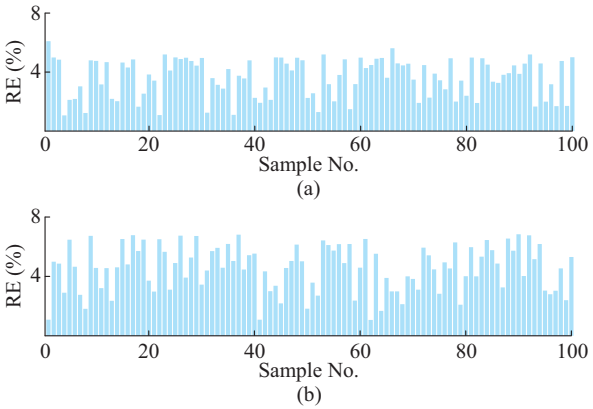

Fig. 12. REs of proposed FAM. (a) Scenario 3. (b) Scenario 4.

From Fig. 12, the REs of the proposed FAM are distributed around 4%, with MAPE being 3.63% and 4.55% in Scenarios 3 and 4, respectively, falling within the acceptable error range. The proposed FAM needs to construct a set of equations by FRAM. Since the FRAM has about a 2% MAPE, some errors are introduced when mapping to the MDI solution. In addition, since ΔP_{d} is nonlinearly related to $H_{\min}$ under the $\Delta f_{\max}$ constraint, the calculation error of FRAM may be scaled when mapping to the MDI solution. Therefore, in Fig. 12, the RE fluctuation of the proposed FAM is slightly larger than that of OSM.

3) Analysis of Calculation Efficiency

Under the same operating condition, the proposed FAM takes about 70 ms for computation, while the OSM takes about 5.5 s. The CCAM takes up to tens or even hundreds of seconds to compute, and further increases with the smaller the iteration step sizes. Corresponding to Fig. 11, the total computation time is 5.24 s and 6.30 s for 100 iterations of the proposed FAM in Scenarios 3 and 4, respectively, while OSM takes 499.82 s and 622.54 s, and CCAM takes 2303.08 s and 2415.12 s ($\mathrm{d}h=0.01$ s, $\varepsilon=0.01$ Hz). Although the computational accuracy of the proposed FAM is slightly reduced, its computational efficiency is significantly higher than that of CCAM and OSM. The proposed FAM takes as little as milliseconds for a single calculation, meeting the demand for fast assessment of power grids in massive operation scenarios while maintaining computational accuracy.

4) Analysis of Inertia Security Boundary

The inertia security boundary in this paper is defined as the boundary consisting of the MDIs required to ensure that the system frequency indicators do not exceed $Rof_{\lim}$ and $\Delta f_{\lim}$ after disturbance, under different frequency security constraints. Based on the proposed FAM, the 3D map of the inertia security boundary can be quickly obtained. The system inertia security boundary under $Rof_{\lim}$ and $\Delta f_{\lim}$ constraints is given in Fig. 13, where a power support of 50 MW with a 1 s delay is set on the load side.

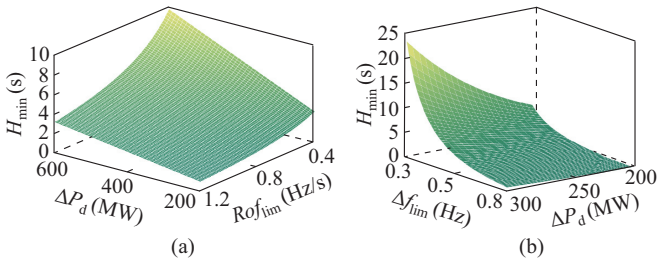

Fig. 13. Inertia security boundary under $Rof_{\lim}$ and $\Delta f_{\lim}$ constraints. (a) Under $Rof_{\lim}$ constraint. (b) Under $\Delta f_{\lim}$ constraint.

From Fig. 13, the larger the disturbance and the tighter the frequency security constraints, the larger the system MDI. By solving the inertia security boundary, the system inertia security situation in different scenarios can be sensed, thus providing a more comprehensive decision-making basis for the operators.

Under the $\Delta f_{\lim}$ constraint, the load-side power support can intercept the frequency nadir, thereby reducing the system demand for inertia. The system inertia security boundaries with load-side power support under different power support sizes ΔP_{L} and different response delays t_0 are given in Fig. 14.

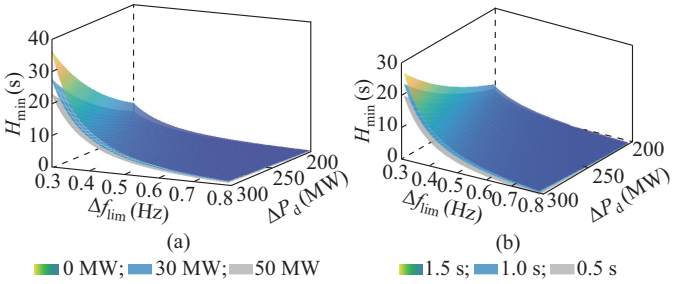

Fig. 14. Inertia security boundary with load-side power support. (a) Under different ΔP_{L} ($t_0=1$ s). (b) Under different t_0 ($\Delta P_{\mathrm{L}}=50$ MW).

The comparative analysis in Fig. 14 shows that as ΔP_L increases and t_0 decreases, the system inertia security boundary shifts downward accordingly, reducing the risk of system inertia overrun. Neglecting the load-side power support, the inertia security boundary will be higher than the actual result. This discrepancy will provide incorrect inertia overrun information to grid operators, posing security risks for inertia resource planning and allocation.

5) Analysis of Renewable Energy Penetration

To analyze the impact of renewable energy penetration on the evaluation accuracy of the proposed FAM, the MAPEs of its sampling calculation results at different renewable energy penetration levels are presented in Fig. 15. In this case, the load side provides 50 MW of power support with a time delay of 1 s, $\Delta f_{\lim}=0.3$ Hz, and the disturbance is sampled 100 times within the range of 100 MW to 400 MW. Since the GFL-IBR lacks grid-forming ability, the GFM-IBR is used to increase the renewable energy penetration.

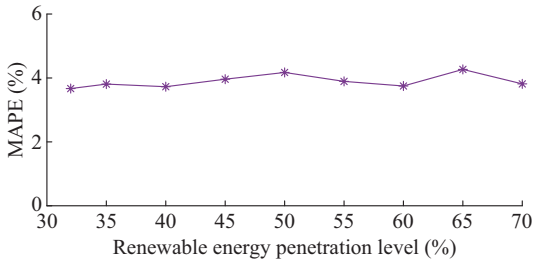

Fig. 15. MAPE at different renewable energy penetration levels.

In Fig. 15, the MAPEs for the sampling calculation results of the proposed FAM are approximately 4% across different renewable energy penetration levels. As the proportion of renewable energy increases, the evaluation accuracy of the proposed FAM remains largely unaffected. Therefore, the proposed FAM can maintain a relatively high computational accuracy for future power systems dominated by grid-forming resources with high renewable energy penetration.

C. A Real Provincial Power Grid in China

1) Analysis of Computational Accuracy

Two scenarios are established. Scenario 5: the load side

provides 100 MW of power support with a time delay of 1 s. The disturbance is sampled 100 times between 2% and 10% of the system capacity. The RE of MFD in Scenario 5 is shown in Fig. 16(a). Scenario 6: the disturbance size is 10% of the system capacity, while the load-side power support is sampled 100 times from 0 MW to 300 MW with a time delay of 1 s. The RE of MFD in Scenario 6 is shown in Fig. 16(b).

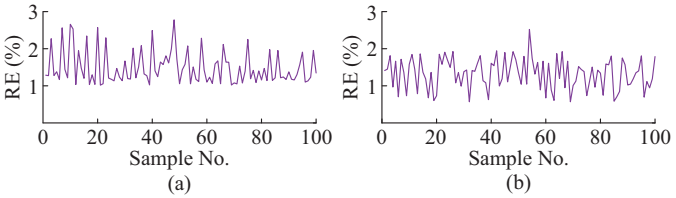

Fig. 16. RE of MFD. (a) Scenario 5. (b) Scenario 6.

Figure 16 shows that the FRAM still demonstrates high computational accuracy in the real provincial power grid. Its MAPEs are 1.49% and 1.32% in Scenarios 5 and 6, respectively. This indicates its capability for fast and accurate calculation for MFD.

To further validate the assessment accuracy and efficiency for MDI, Fig. 17(a) illustrates the RE of MDI corresponding to 100 random samples of the disturbance between 5% and 6% of the system capacity, with 300 MW of power support on the load side (Scenario 7). Figure 17(b) presents the RE of MDI when the disturbance is 6% of the system capacity and the load-side power support is randomly sampled 100 times between 400 MW and 500 MW (Scenario 8). The load-side response delay is set to be 1 s in both scenarios, and $\Delta f_{\text{lim}} = 0.4$ Hz.

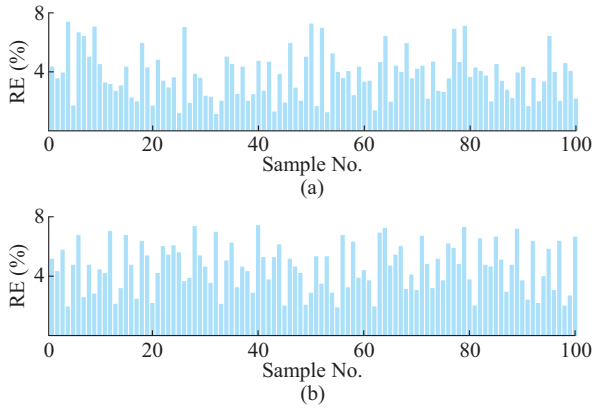

Fig. 17. RE of MDI. (a) Scenario 7. (b) Scenario 8.

Figure 17 shows that the REs of MDI are distributed around 4%, and its MAPEs in Scenarios 7 and 8 are 3.76% and 4.61%, respectively. The proposed FAM for MDI maintains high computational accuracy in the provincial large-scale grid and remains unaffected by the system scale.

2) Analysis of Computational Efficiency

Corresponding to the two scenarios in Fig. 17, the total computation time of the proposed FAM is only 4.30 s and 8.01 s, while the OSM costs up to 603.88 s and 730.06 s, and the CCAM costs up to 2436.95 s and 2594.39 s (dh = 0.01 s, $\varepsilon = 0.01$ Hz). The efficiency of the proposed FAM is significantly higher than that of OSM and CCAM. Additionally, its average computation time remains around 70 ms, independent of the system scale, demonstrating its high computational efficiency even in large power grids.

The validation and analysis of calculation accuracy and efficiency show that the proposed FAM for MDI significantly improves the MDI assessment efficiency while maintaining high computational accuracy. Moreover, both computational efficiency and assessment accuracy remain unaffected by the system scale. As the system scale and operational scenarios increase, the advantage of the proposed FAM in computational efficiency will be more prominent. Additionally, the modeling and solution of the proposed FAM are straightforward to implement, making it more applicable than traditional MDI assessment methods.

3) Analysis of Inertia Security Boundary

In real power grids, decision-makers need to focus on the system inertia security boundary under Rof_{lim} and Δf_{lim} constraints to obtain more comprehensive inertia overrun information. When the system inertia falls below the inertia security boundary, it indicates that the inertia cannot meet the system demand, and the system is in an inertia overrun state. Figure 18 gives the system inertia security boundary under the two constraints, where the load side provides 300 MW of power support with a response delay of 1 s .

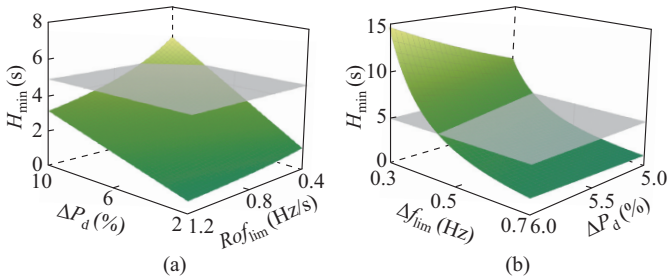

Fig. 18. Inertia security boundary under Rof_{lim} and Δf_{lim} constraints. (a) Under Rof_{lim} constraint. (b) Under Δf_{lim} constraint.

To further analyze the effects of load-side power support size and response delay on MDI, the system inertia security boundary is given in Fig. 19 under different power support sizes ΔP_{L} and response delays t_0.

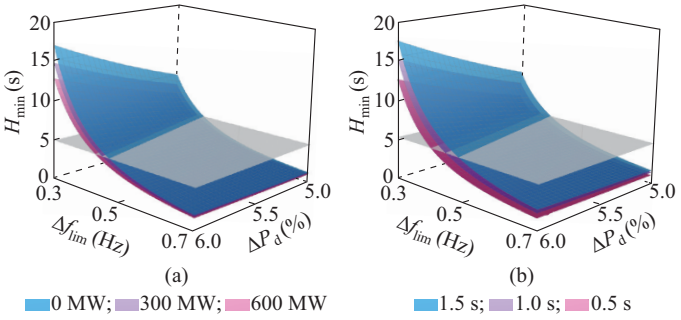

Fig. 19. Inertia security boundary under different power support sizes and response delays with load-side power support. (a) Under different ΔP_{L} (t_0 = 1 s). (b) Under different t_0 ($\Delta P_{\text{L}} = 300$ MW).

From Figs. 18 and 19, as the disturbance increases and the frequency security constraints tighten, the system MDI rises and exceeds its inertia level. Using the proposed FAM, the system inertia overrun information in different operation scenarios can be quickly obtained, thus providing a fast and comprehensive basis for sensing inertia security situation, resource planning, and allocation. In addition, the inertia support effect provided by the load-side resources in large power grids cannot be neglected. With the increase of load-side power support and response speed, the system inertia security boundary shifts downward, reducing the risk of inertia overrun.

VI. Conclusion

This paper proposes an FAM for MDI in power systems to address the problems of complex modeling and low computational efficiency in existing MDI assessment methods. Theoretical analysis and case studies demonstrate that:

1) The proposed FAM for MDI can significantly improve the computational efficiency while maintaining high computational accuracy. It achieves millisecond-level computation, enabling fast assessment of MDI. Moreover, its computational accuracy and efficiency remain unaffected by system scale, making its advantage more prominent for large-scale power grids and massive operation scenarios.

2) If the inertia support capability of load-side resources in the system is neglected, the MDI assessment results will be larger than the actual results, leading to incorrect decision-making for inertia security situation sensing, resource planning, and allocation. The proposed FAM for MDI can consider the inertia support capacity of load-side resources, yielding results that better match actual grid conditions.

3) As the disturbance increases and the frequency security constraints tighten, the MDI in power systems also rises. The system inertia overrun information in different operation scenarios can be quickly obtained through the proposed FAM. Furthermore, as the load-side power support and response speed increase, the system inertia security boundary expands, and the risk of inertia overrun is correspondingly reduced.

In the future, we will further investigate the proposed FAM of MDI in power system considering the spatio-temporal distribution of inertia.

References

[1] E. Heylen, F. Teng, and G. Strbac, "Challenges and opportunities of inertia estimation and forecasting in low-inertia power systems," *Renewable and Sustainable Energy Reviews*, vol. 147, p. 111176, Sept. 2021.

[2] ENTSO-E. (2017, Sept.). Task force code–system dynamic issues for the synchronous zone of continental Europe. [Online]. Available: https://eepublicdownloads.entsoe.eu/clean-documents/SOC%20documents/Regional_Groups_Continental_Europe/2017/170926_RG_CE_TOP_08_1_D_1_SPD_Codes_TF_v5_System_Dynamic_Issues_for_CE.pdf

[3] B. Tan, J. Zhao, M. Netto *et al*., "Power system inertia estimation: review of methods and the impacts of converter-interfaced generations," *International Journal of Electrical Power & Energy Systems*, vol. 134, p. 107362, Jan. 2022.

[4] H. Sun, T. Sun, Q. Guo *et al*., "Analysis on blackout in Great Britain power grid on August 9th, 2019 and its enlightenment to power grid in China," *Proceedings of the CSEE*, vol. 39, no. 21, pp. 6183-6191, Nov. 2019.

[5] R. Yan, N. A.-Masood, T. K. Saha *et al*., "The anatomy of the 2016 South Australia blackout: a catastrophic event in a high renewable network," *IEEE Transactions on Power Systems*, vol. 33, no. 5, pp. 5374-5388, Sept. 2018.

[6] B. Tan and J. Zhao, "Data-driven time-varying inertia estimation of inverter-based resources," *IEEE Transactions on Power Systems*, vol. 38, no. 2, pp. 1795-1798, Mar. 2023.

[7] ENTSO-E. (2021, Nov.). The inertia challenge in Europe–present and long-term perspective. [Online]. Available: https://eepublicdownloads.blob. core. windows. net/public-cdn-container/tyndp-documents/TYNDP2020/Forconsultation/200611_TYNDP2020_IR_Inertia_forconsultation.pdf

[8] WECC. (2021, May). Changes in system inertia. [Online]. Available: https://www.wecc.org/wecc-document/2441

[9] G. Zhang, J. Ren, Y. Zeng *et al*., "Security assessment method for inertia and frequency stability of high proportional renewable energy system," *International Journal of Electrical Power & Energy Systems*, vol. 153, p. 109309, Nov. 2023.

[10] C. He, J. Zhao, S. Huang *et al*., "Wind-storage combined system flexible inertia control strategy based on minimum system inertia demand estimation," in *Proceedings of 2024 4th Power System and Green Energy Conference*, Shanghai, China, Aug. 2024, pp. 764-769.

[11] H. Gu, R. Yan, and T. K. Saha, "Minimum synchronous inertia requirement of renewable power systems," *IEEE Transactions on Power Systems*, vol. 33, no. 2, pp. 1533-1543, Mar. 2018.

[12] Z. Xie and Y. Tang, "Evaluation of minimum inertia requirement of power system considering source-load inertia characteristics," *Automation of Electric Power Systems*, vol. 48, no. 10, pp. 66-77, May 2024.

[13] B. Wang, H. Sun, W. Li *et al*., "Minimum inertia estimation of power system considering dynamic frequency constraints," *Proceedings of the CSEE*, vol. 42, no. 1, pp. 114-127, Jan. 2022.

[14] Y. Chen, S. Feng, G. You *et al*., "Calculation for minimum inertia of power system based on improved GWO algorithm," in *Proceedings of 2022 IEEE 6th Conference on Energy Internet and Energy System Integration*, Chengdu, China, Nov. 2022, pp. 2931-2937.

[15] X. Guo, G. Yang, J. Fei *et al*., "Assessment of inertia demand in power system considering spatio-temporal characteristics and multi-index constraints," *High Voltage Engineering*, vol. 50, no. 1, pp. 148-156, Jan. 2024.

[16] C. Liu, Z. Lin, F. Ouyang *et al*., "Minimum inertia requirement evaluation method of power systems considering frequency stability constraints and spatial distribution characteristics," in *Proceedings of 2023 IEEE 7th Conference on Energy Internet and Energy System Integration*, Hangzhou, China, Dec. 2023, pp. 1-6.

[17] W. Zhang, Y. Wen, and C. Y. Chung, "Inertia security evaluation and application in low-inertia power systems," *IEEE Transactions on Power Systems*, vol. 40, no. 2, pp. 1725-1737, Mar. 2025.

[18] T. Zhou, Z. Chen, Y. Wang *et al*., "Evaluation of minimum inertia in power systems considering frequency response of induction machines," *Power System Protection Control*, vol. 50, no. 20, pp. 22-31, Oct. 2022.

[19] L. Chen, X. Wang, Y. Min *et al*., "Modelling and investigating the impact of asynchronous inertia of induction motor on power system frequency response," *International Journal of Electrical Power & Energy Systems*, vol. 117, p. 105708, May 2020.

[20] P. M. Anderson and A. A. Fouad, *Power System Control and Stability*. New York, USA: Wiley-IEEE Press, 2002.

[21] X. Wang, W. Li, J. Shen *et al*., "Reduced-order bus frequency response model for bulk power systems," *Journal of Modern Power Systems and Clean Energy*, vol. 13, no. 4, pp. 1127-1138, Jul. 2025.

[22] J. Zhao, Y. Tang, and V. Terzija, "Robust online estimation of power system center of inertia frequency," *IEEE Transactions on Power Systems*, vol. 34, no. 1, pp. 821-825, Jan. 2019.

[23] L. Liu, W. Li, Y. Ba *et al*., "An analytical model for frequency nadir prediction following a major disturbance," *IEEE Transactions on Power Systems*, vol. 35, no. 4, pp. 2527-2536, Jul. 2020.

[24] C. Jin, W. Li, J. Shen *et al*., "Active frequency response based on model predictive control for bulk power system," *IEEE Transactions on Power Systems*, vol. 34, no. 4, pp. 3002-3013, Jul. 2019.

[25] Z. Li, L. Guo, S. Yu *et al*., "An efficient full-response analytical model for probabilistic production simulation in fast frequency response reserve planning," *Energy*, vol. 273, p. 127268, Jun. 2023.

[26] Q. Shi, F. Li, and H. Cui, "Analytical method to aggregate multi-machine SFR model with applications in power system dynamic studies," *IEEE Transactions on Power Systems*, vol. 33, no. 6, pp. 6355-6367, Nov. 2018.

[27] D. Sun, H. Liu, S. Gao *et al*., "Comparison of different virtual inertia

control methods for inverter-based generators," *Journal of Modern Power Systems and Clean Energy*, vol. 8, no. 4, pp. 768-777, Jul. 2020.
[28] E. A. S. Ducoin, Y. Gu, B. Chaudhuri *et al*., "Analytical design of contributions of grid-forming and grid-following inverters to frequency stability," *IEEE Transactions on Power Systems*, vol. 39, no. 5, pp. 6345-6358, Sept. 2024.
[29] C. Li, Y. Yang, Y. Li *et al*., "Modeling for oscillation propagation with frequency-voltage coupling effect in grid-connected virtual synchronous generator," *IEEE Transactions on Power Electronics*, vol. 40, no. 1, pp. 82-86, Jan. 2025.
[30] M. Choopani, S. H. Hosseinian, and B. Vahidi, "New transient stability and LVRT improvement of multi-VSG grids using the frequency of the center of inertia," *IEEE Transactions on Power Systems*, vol. 35, no. 1, pp. 527-538, Jan. 2020.
[31] H. Sun, B. Wang, W. Li *et al.*, "Research on inertia system of frequency response for power system with high penetration electronics," *Proceedings of the CSEE*, vol. 40, no. 16, pp. 5179-5191, Aug. 2020.
[32] R. Bhana and T. J. Overbye, "The commitment of interruptible load to ensure adequate system primary frequency response," *IEEE Transactions on Power Systems*, vol. 31, no. 3, pp. 2055-2063, May 2016.
[33] C. Miao, Y. Jiang, L. Shin *et al*., "Capability assessment and application of fast frequency response load participating in inertia auxiliary service," *Automation of Electric Power Systems*, vol. 48, no. 16, pp. 99-108, May 2024.
[34] I. Egido, F. Fernandez-Bernal, P. Centeno *et al*., "Maximum frequency deviation calculation in small isolated power systems," *IEEE Transactions on Power Systems*, vol. 24, no. 4, pp. 1731-1738, Nov. 2009.
[35] P. Yi, Z. Jing, F. Xu *et al*., "Calculation of the critical inertia of a power system considering frequency security constraints," *Journal of Tsinghua University (Science & Technology)*, vol. 62, no. 10, pp. 1721-1729, Oct. 2022.
[36] Q. Ding, X. Zhang, N. Zhang *et al*. (2024, Aug.). A joint planning and configuration method for power system inertia and primary frequency regulation reserve considering extreme events. [Online]. Available: http://kns.cnki.net/kcms/detail/11.2107.TM.20240829.1246.008.html

Qili Ding received the B. S. degree in electrical engineering from Dalian Maritime University, Dalian, China, in 2022. He is currently pursuing the Ph.D. degree in School of Electrical Engineering, Dalian University of Technology, Dalian, China. His research interests include power system frequency stability analysis and control.

Xinggan Zhang received the B.S. degree in electrical engineering from Dalian University of Technology, Dalian, China, in 2024. He is currently pursuing the M. S. degree in School of Electrical Engineering, Dalian University of Technology. His research interests include power system frequency stability analysis and control.

Zifeng Li received the M.S. degree from Northeast Electric Power University, Jilin, China, in 2019, and the Ph. D. degree from Dalian University of Technology, Dalian, China, in 2023. He is currently working in Dalian Electric Power Supply Company of State Grid Liaoning Electric Power Supply Co., Ltd., Dalian, China. His research interests include power system reserve planning and optimal control of active frequency response.

Xiangxu Wang received the B.S. and Ph.D. degrees in electrical engineering from Dalian University of Technology, Dalian, China, in 2019 and 2025, respectively. He is currently working in the Electric Power Research Institute of State Grid Liaoning Electric Power Supply Co., Ltd., Shenyang, China. His research interests include modeling, analysis, and simulation of frequency response in power system.

Weidong Li received the B.S., M.S., and Ph.D. degrees in electrical engineering from Xi'an Jiaotong University, Xi'an, China, Northeast Electric Power University, Jilin, China, and Harbin Institute of Technology, Harbin, China, in 1985, 1988, and 1997, respectively. Now, he is a Professor of electrical engineering with Dalian University of Technology, Dalian, China, where he served as the Dean of School of Electrical Engineering, from 2011 to 2016. His research interests include power system automation, frequency stability analysis, and control of new power system.